Fe^{+3}-doped Anatase TiO_2 with d-d Transition, Oxygen Vacancies and Ti^{+3} Centers: Synthesis, Characterization, UV-vis Photocatalytic and Mechanistic Studies

Hayat Khan*, Imran Khan Swati

Supplementary Information

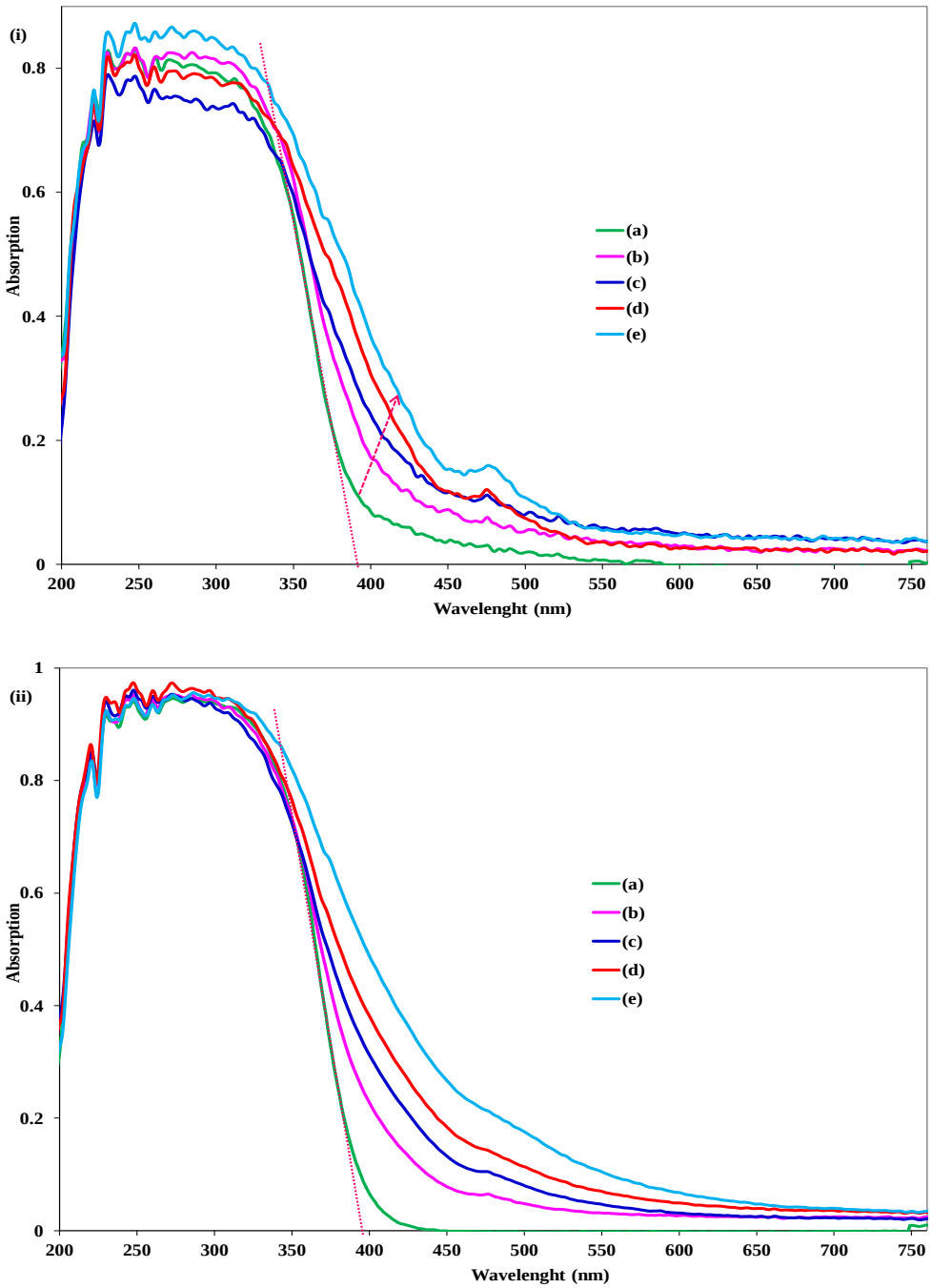

Figure S1 DRS UV-vis absorption spectra of the powders calcined at 300 (i) and 500 ^{o}C (ii), the samples are (a) T, (b) TFe_{200}, (c) TFe_{100}, (d) TFe_{50} and (e) TFe_{25}.

1.1. Raman Spectroscopy

Raman spectroscopy experiments were carried out to further confirm the structural phases of undoped and doped TiO_2 nanoparticles calcined at 300 ^oC (Figure S2). As can be seen the Raman features recorded for undoped TiO_2 confirms the presence of basically the anatase TiO_2 crystalline phase, as evidence by the presence of mainly five Raman peaks corresponding to the six active modes expected for the anatase tetragonal structure ($3E_g$, $2B_{1g}$, $1A_{2g}$). [1-3] The Raman bands were observed at 144, 196.5, 396.1, 515.7 and 639.1 cm^{-1} for undoped TiO_2, Fe^{+3} doped nanoparticles exhibited a Raman peak pattern similar to that of undoped TiO_2 (anatase structured). Any peak related to iron oxide (α-Fe_2O_3, $TiFe_3O_4$) were not detected, this means that Raman spectral results are in accordance with powder XRD observation, moreover, Fe-TiO_2 nanoparticles preserved the anatase structure, which indicates that Fe^{+3} dopant is substitutionally incorporated into the TiO_2 frame work replacing Ti^{+4} cations. However, it was observed that the Raman band at 144 cm^{-1} ($1\text{-}E_g$) tend to shift to the high wavenumber with peak broadening as the iron content increases, as shown in Figure 8 insert. The unusual broadening and shifts of the Raman bands are associated with changes in structure, particle size, calcination temperature, nonstoichiometery and nature of defects, any dominant change in the above parameters firstly effect the lowest frequency vibrational mode at 144 cm^{-1} [2,3]. From XRD analysis it is clear that TiO_2 crystallite size decrease with increase in dopant amount, this happens due to the change in force constant and vibrational amplitude caused by the volume contraction effect (as a result of difference in the ionic radii of Fe^{+3} and Ti^{+4}). In addition, PL analysis showed oxygen vacancies induced defects resulting into the change in oxygen stoichiometry for the TiO_2 nanoparticles with different Fe^{+3} content. Thus, it can be argued that the present shifting in the Raman band ($1\text{-}E_g$) is due to the change in particle size and oxygen vacancies as a result of Fe^{+3} doping in TiO_2.

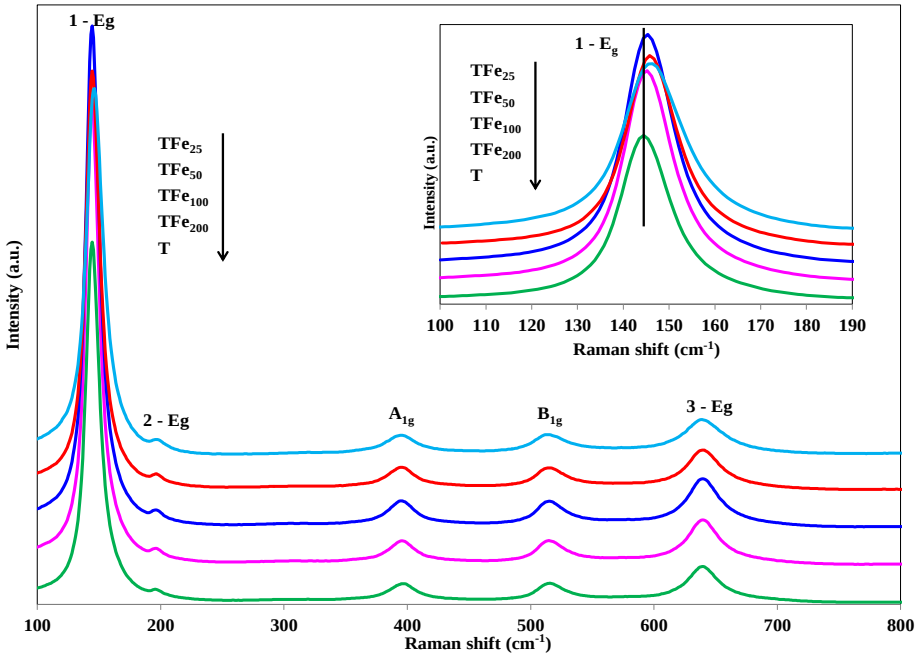

Figure S2. Raman spectra of the indicated samples calcined at 500 ^{o}C; (insert) Raman shift in 1-E_g mode.

1.2. N_2 Physisorption

N_2 adsorption-desorption isotherms measured at 77 K were compared to investigate the microstructural changes due to the presence of Fe^{+3} in TiO_2 structure. Figure S3 shows the physisorption isotherms of undoped (T) and doped titania (TFe_{50}) calcined at 500 ^{o}C, while the insert display the pore size distribution curve measured by BJH (Barret-Joyner-Halender) method. All the samples showed type-IV adsorption-desorption isotherm according to IUPAC classification with a H4 hysteresis loop caused by capillary condensations within the mesopores. The textural parameters shown in Table S1 illustrates that compared to undoped TiO_2, doped powders have high specific surface area, the BET (Brunauer-Emmett-Teller) results are consistent with the XRD analysis which indicates that Fe^{+3} ions results in the inhibition of crystallite growth. The Fe^{+3}-doped TiO_2 nanoparticles had a uniform pore size distribution (Table S1), the pore size followed a decreasing trend with increase in Fe content, which resulted in the increase of S_{BET}. Moreover, in all the catalyst powders, external surface area (S_{EXT}) is greater than specific surface area (S_{BET}), this means that the solid contains macropores. Therefore, it can be concluded that Fe-TiO_2 catalysts have large surface area consisting of mesoporous and macroporous structure and wide pore size distribution, which will promote

adsorption, desorption and diffusion of reactants and products [4], thus high photocatalytic activity of doped samples is expected. Table S1 also showed that a decrease in specific surface area is observed with increase in annealing temperature, because TiO_2 crystallite size increases with increase in calcination temperature.

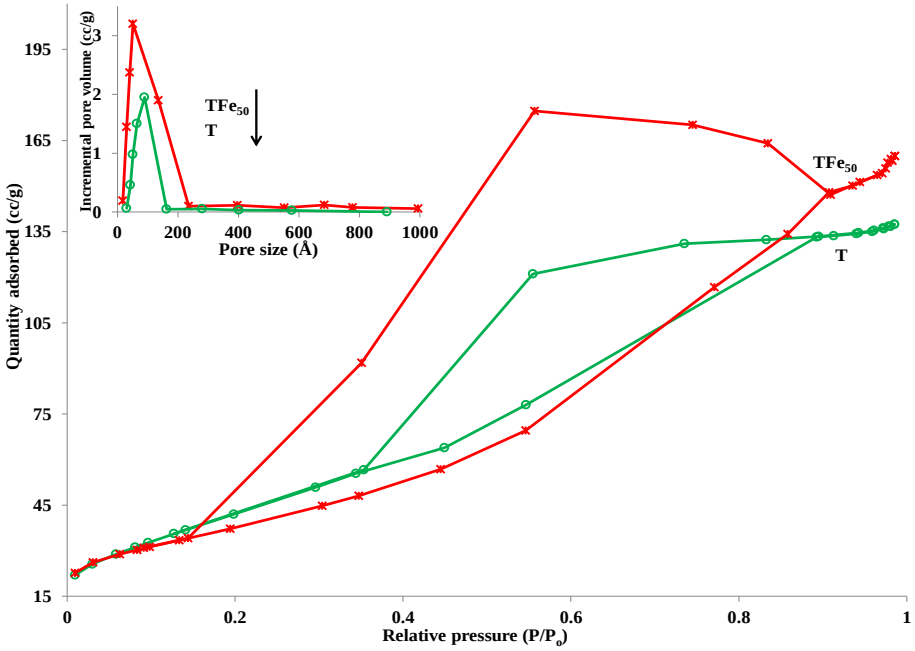

Figure S3 N_2 adsorption-desorption isotherm, (insert) BJH pore size distribution of the indicated samples calcined at 500 ^oC.

Table S1. Comparison of BET specific surface area (S_{BET}), external surface area (S_{EXT}), mesopores volume, BJH pore size and BJH pore volume of undoped and Fe^{+3}-doped TiO_2 powders, calcined at 300 and 500 ^oC.

Catalyst sample	Temperature (^oC)	S_{BET} (m^2/g)	S_{EXT} (m^2/g)	Mesopores volume (cm^3/g)	BJH pore size (Å)	BJH pore volume (cc/g)
T		178	247	0.186	147.0	2.0
TFe_{200}		166	230	0.102	136.0	2.1
TFe_{100}	300	203	273	0.187	161.0	2.6
TFe_{50}		236	331	0.203	216.0	3.2
TFe_{25}		262	367	0.245	187.0	2.3
T		157	224	0.156	95.0	1.7
TFe_{200}		143	203	0.121	111.0	2.0
TFe_{100}	500	182	237	0.157	127.0	2.1
TFe_{50}		201	284	0.172	161.0	2.5
TFe_{25}		215	313	0.187	142.0	1.8

Table S2. Photocatalytic degradation of different pollutants in the presence of Fe^{+3}-TiO_2 (prepared by different methods) under UV and visible light irradiation

Synthesis method	Light source / power (W) / optimum amount of photocatalyst powder	Pollutant	Concentration	Volume / catalyst (g/L)	% degradation* / time (min)
Hydrothermal [5]	UV – 365 nm / unknown / 3.0 at.% Simulated solar light / unknown / 3.0 at.%	Rhodamine B	10 μM	40 ml / 0.05	17/120 14/120
Sol-gel with hydrothermal [4]	UV high pressure Hg lamp – 365nm / 300 / 0.04 mass% Visible light (>365 nm) using glass filter as cut-off / 300 / 0.15 mass%	Active yellow XRG	100 mg/L	60 mL /0.06	80/60 82/420
Microemulsion [6]	UV high pressure Hg lamp – 365 nm / 500 / 0.7 wt.% No visible light activity experiment were performed	Phenol	500 ppm	1L / 0.5	65** / 300
Precipitation hydrothermal [7]	UV high pressure Hg lamp (365 nm) / 300 / 0.5 Halogen lamp as visible light (>420 nm) using glass optical filter as cut-off / 1000 / 0.5	Rhodamine B	20 mg/L	50 mL / 0.05	75 / 120 85 / 240
Co-precipitation [8]	Osram Xenon short arc optic lamp was used as simulated solar light / 1000 / 0.1 wt.%	Methylene blue	0.02 mM	200 mL / 0.24	80 / 180
Sol-gel [9]	High pressure Hg lamp (> 400 nm) with cut-off filter was used as visible light source / 125 / 0.5% (atom ratio)	Methylene blue	10 mg/L	100 mL / 0.4	70 / 180
Sol-gel [10]	Xenon lamp, UV (300-380 nm) / 300 / 0.5 mol ratio Same lamp was used for visible light using cut-off filter (>420 nm) / 300 / 1.0 mol ratio	Methyl orange	0.025 mM	100 mL / 1.0	44 / 60 25 / 60
Incipient wet impregnation [11]	No UV experiments were performed Black light fluorescence lamps / 5 x 8 /	4-Nitrophenol	0.001 mol/L	0.6 L / 0.2	80 / 120

	0.25 wt%				
Solution combustion method [12]	UV medium pressure Hg lamp (360 nm) / 125 / 7.5 at.% Visible experiments were carried out with direct sun light having average intensity of 0.753 KW/m^2 / 7.5 at.%	4-Nitrophenol	0.5 mM	190 mL / 1.0 0.4 L / 1.0	90 / 60 30 / 200
Metallorganic chemical vapor deposition (MOCVD) [13]	UV Hg lamp (365 nm) / 100 / 1.0 at.% No visible light activity experiments are performed	2-Chlorophenol	50 mg/L	9.42 L / 1.0	100 / 120
Wet impregnation [14]	UV medium-pressure Hg lamp / 125 / 1.0 mol of Fe ions over 100 mol of Ti ions No visible light activity experiments were performed	4-Nitrophenol	20 mg/L	0.5 L / 1.4	90 / 350
Coprecipitation [15]	UV lamp – 300-400 nm / 6 / 0.5 v/v% No visible light experiments were performed	Methylene blue	46 mg/L	50 mL / 0.01	39 / 300
Sol-gel – present work	UV light – 254 nm / 11 / 50 mol ratio Hg-medium pressure lamp as visible light – 420-660 nm / 180 / 50 mol ratio	Methylene blue 4-Chlorophenol	7.5 mg/L 35 mg/L	2.4 L / 0.1 0.85 L / 0.1	98 / 60 90 / 10

* Approximated value taken by reading the C/C_o figure

** Approximated value taken by reading the $[TOC]/[TOC]_o$ figure

References

1. Zhang, W. F.; He, Y. L.; Zhang, M. S.; Yin, Z.; Chen, Q., Raman scattering study on anatase TiO_2 nanocrystals. *J.Phys. D: Appl. Phys*. **2000,** 33, 912-916.
2. M.Popa; Diamandescu, L.; Vasiliu, F.; Teodorescu, C. M.; Cosoveanu, V.; Baia, M.; Feder, M.; Baia, L.; Danciu, V., Synthesis, structural characterization, and photocatalytic properties of iron-doped TiO_2 aerogels. *J. Mater. Sci.* **2009,** 44, 358-364.
3. Santara, B.; Pal, B.; Giri, P. K., Signature of strong ferromagnetism and optical properties of Co doped TiO_2 nanoparticles. *J. Appl. Phys.* **2011,** 110, 114322-114328.
4. Zhu, J.; Chen, F.; Zhang, J.; Chen, H.; Anpo, M., Fe^{3+}-TiO_2 photocatalysts prepared by combining sol–gel method with hydrothermal treatment and their characterization. *J. Photochem. Photobiol. A: Chem.* **2006,** 180, 196-204.
5. Yang, M.; Hume, C.; Lee, S.; Son, Y. H.; Lee, J. K., Correlation between photocatalytic efficacy and electronic band structure in hydrothermally grown TiO_2 nanoparticles. *J. Phys. Chem. C.* **2010,** 114, 15292-15297.
6. Adan, C.; Bahamonde, A.; Fernandez, M. F.; Arias, A. M., Structure and activity of nanosized iron-doped anatase TiO_2 catalysts for phenol photocatalytic degradation. *Appl. Catal. B: Environ.* **2007,** 72, 11-17.
7. Cong, Y.; Zhang, J.; Chen, F.; Anpo, M.; He, D., Preparation, photocatalytic activity, and mechanism of nano-TiO_2 co-doped with nitrogen andiIron (III). *J. Phys. Chem. C.* **2007,** 111, 10618-10623.
8. Ganesh, I.; Kumar, P. P.; Gupta, A. K.; Sekhar, P. S. C.; Radha, K.; Padmanabham, G.; Sundararajan, G., Preparation and characterization of Fe-doped TiO_2 powders for solar light response and photocatalytic applications. *Processing and Application of Ceramics.* **2012,** 6, 21-36.
9. Guo, J.; Gan, Z.; Lu, Z.; Liu, J.; Xi, J.; Wan, Y.; Le, L.; Liu, H.; Shi, J.; Xiong, R., Improvement of the photocatalytic properties of TiO_2 by (Fe+Mo) co-doping—A possible way to retard the recombination process. *J. Appl. Phys.* **2013,** 114, 104903-104909.
10. Qamar, M.; Merzougui, B.; Anjum, D.; Hakeem, A. S.; Yamani, Z. H.; Bahnemann, D., Synthesis and photocatalytic activity of mesoporous nanocrystalline Fe-doped titanium dioxide. *J. Catal. Today* **2014,** 230, 158-165.
11. Yalcın, Y.; Kılıc, M.; Cınar, Z., Fe^{+3} doped TiO_2: A combined experimental and computational approach to the evaluation of visible light activity. *Appl. Catal. B: Environ.* **2010,** 99, 469-477.
12. Nagaveni, K.; Hegde, M. S.; Madras, G., Structure and photocatalytic activity of $Ti_{1-x}M_xO_{2\pm\delta}$ (M = W, V, Ce, Zr, Fe, and Cu) synthesized by solution combustion method. *J. Phys. Chem. B.* **2004,** 108, 20204-20212.
13. Shah, S. I.; Li, W.; Huang, C. P.; Jung, O.; Ni, N., Study of Nd^{3+}, Pd^{2+}, Pt^{4+}, and Fe^{3+} dopant effect on photoreactivity of TiO_2 nanoparticles. *Proceedings of the National Academy of Sciences.* **2002,** 99, 6482-6486.
14. Paola, A. D.; Marci, G.; Palmisano, L.; Schiavello, M.; Uosaki, K.; Ikeda, S.; Ohtani, B., Preparation of polycrystalline TiO_2 photocatalysts impregnated with various transition metal Ions: Characterization and photocatalytic activity for the degradation of 4-Nitrophenol. *J. Phys. Chem. B.* **2001,** 106, 637-645.
15. Molea, A.; Popescu, V.; Rowson, N. A.; Cojocaru, I.; Dinescu, A.; Dehelean, A.; Lazar, M., Correlation of physicochemical properties with the catalytic performance of Fe-doped titanium dioxide powders. *J. Ind. Eng. Chem. Res.* **2015,** 54, 7346-7351.